Adaptation of the PTV method for droplets evaporating in vicinity of a flame

Gaël Parant, Laurent Zimmer, Antoine Renaud, Franck Richecoeur

To cite this version:

Gaël Parant, Laurent Zimmer, Antoine Renaud, Franck Richecoeur. Adaptation of the PTV method for droplets evaporating in vicinity of a flame. 2021. hal-03364134v1

HAL Id: hal-03364134
https://hal.science/hal-03364134v1

Preprint submitted on 4 Oct 2021 (v1), last revised 24 Nov 2023 (v3)

Noname manuscript No.
(will be inserted by the editor)

Adaptation of the PTV method for droplets evaporating in vicinity of a flame

Gaël Parant*, **Laurent Zimmer**, **Antoine Renaud**,
Franck Richecoeur

Received: date / Accepted: date

Abstract Measuring the time and length of evaporation of fuel droplets provides a better understanding of the dynamics of spray dynamics. However, when a drop evaporates it is increasingly difficult to detect them and therefore it is difficult to track them with a PTV algorithm. To solve this problem, we have adapted classical PTV algorithms by exploiting the image of the drop at frame N to find it in frame N+1. The images collected for the PTV are also used to measure the physical size of the drops by ILIDS. We applied this new algorithm to a counter-current burner with dodecane droplets evaporating on an air-methane flame. The velocity field surrounding the droplets was measured by PIV and the temperature field by Rayleigh measurement. The treatment of the data collected during the experiment shows that the PTV algorithm succeeded in following the droplets during all their evaporation phase which would have been very difficult for a classical PTV algorithm. Moreover, since droplets evaporate in a high temperature environment, it is impossible to track their physical size from ILIDS, therefore the follow-up of the droplet during its all evaporating phase was key.

1 Introduction

Nowadays, drops and sprays are widely used for material synthesis or liquid fuel injection in internal combustion engines. To analyze the mass exchange between the environment and the droplets, the evaporation length and delay are key quantities to measure.

A direct measurement by filming the evaporation of the drops provides very good results [13, 19, 3, 14, 5]. Even when the drop evolves in an environment with an inhomogeneous temperature, it is possible to obtain results with a high degree of accuracy [20]. However, this diagnosis quickly reaches its limits when the trajectory of the droplets is not known in advance or when the droplets become very small. For small droplets (a few tens of microns) with arbitrary trajectories, new strategies must be implemented.

Interferometric measurements were used to track the position of the droplets while measuring their diameter. This technique, introduced by Konig[8], taken up and improved since[18, 11, 10, 7] and also formalized by Damaschke[4], allows to trace the diameter of the droplets by measuring the number of interference fringes resulting from the interaction between the laser and the droplets. This allowed Park[15] to understand the spatial distribution of the droplets thanks to a simultaneous measurement of their position and their diameter. This same technique was used to measure the evaporation of droplets near a flame by Thimothee[21], showing that it is possible to use this diagnosis in the presence of burnt gases. Wu[23] has taken this diagnostic further by using the fringe position to estimate a nanometric variation of the drop size. Indeed, in the limit of a small change in diameter, the number of bangs hardly changes, but the position of the fringes varies proportionally to the diameter.

---

* gael.parant@centralesupelec.fr

EM2C, CNRS, CentraleSupélec, Université Paris Saclay, 3 Rue Joliot-Curie, 91190 Gif-sur-Yvette, France

When the evaporation takes place in a constraining environment, with a high ambient temperature for example, the diameter decreases rapidly and consequently the number as well as the position of the bangs are not stable, making it impossible to use interferometric measurements. Thus, an evaporation will be said to be *rapid* if it is not possible to correctly identify the interference fringes on the camera image because of a too important movement during the exposure time. To measure the time and distance in this type of evaporation, it becomes important to follow the droplets during their whole life.

However, the light intensity decreases sharply as the diameter decreases [17] and thus finding droplets at the end of their life becomes a very difficult task. Classical PTV algorithms, to track droplets, are done in two steps [16]: droplets are detected on each image and then the trajectories are reconstructed from the detected droplets. These algorithms are not usable on the droplets at the end of their life which will be almost undetectable because of their weak intensity. We therefore risk missing a whole part of the evaporation phase.

To exploit most of the signal received by the camera, this paper proposes to adapt the PTV algorithms to follow the droplets that evaporate *rapidly*.

The PTV algorithm presented in this article uses the maximum information of each drop at image N to find it at image N+1. Thus, droplets of about ten microns, which are difficult to see, will be followed throughout their evaporation phase because the algorithm will know where to look for them and what they look like.

First, the details of this new PTV algorithm will be described. Then, we will present an application case. This one will be fully characterized in order to show that in this configuration the drops evaporate *rapidly*. Finally, the results of the PTV tracking will be presented and the physical orders of magnitude will be discussed.

2 Droplet tracking, diameter measurement and evaporation

2.1 Droplet image and diameter measurement

Before going into the details of the algorithm, let's start by recalling the theory behind the PTV and ILIDS.

PTV tracking is a post-processing that allows to track particles - here droplets - on consecutive images taken with a small time interval. The algorithm takes in a movie of these particles and an indication of what it should look for and deduces the trajectories of these particles.

The ILIDS, on the other hand, measures the physical size of the droplets. According to Mie's theory, when a laser illuminates a droplet, the rays of the first-order refraction and the reflection on the droplet interfere with each other. This interference can be measure at a precise angle. Damaschke [4] introduced the following formula to trace the physical size of droplets:

$$N_f = D\frac{\arcsin\left(d_a/2z_l\right)}{\lambda}\left(\cos\left(\frac{\phi}{2}\right)+\frac{n\sin\left(\frac{\phi}{2}\right)}{\sqrt{n^2+1-2n\cos\left(\frac{\phi}{2}\right)}}\right) \tag{1}$$

where N_f is the number of fringes, d is the droplet diameter, d_a is the lens aperture diameter, z_l is the distance from the lens to the light sheet, λ is the light source wavelength, ϕ is the angle of collection relative to the laser sheet and n is the refractive index of the liquid.

In order to limit the superposition of the droplets on the camera, a particular mask is placed on the camera which changes the droplets' image [2]. The resulting image is illustrated on the figure 2. The PTV algorithm will seek for this pattern. Compared to the classical compressed ILIDS[10, 7], this mask limits the superposition of droplets on the same line and allows to measure precisely the apparent diameter. This mask has no influence on the number of visible fringes.

In the rest of this section, the PTV algorithm is detailed and the ILIDS measurement is presented.

2.2 Structure of the PTV algorithm

The PTV algorithm goes through the images collected by the camera to find and track the droplets in each frame. Figure 1 shows how the algorithm works from the droplets found at frame N to find the droplets at frame N+1. First of all, the scheme is detailed and then the initialisation of the algorithm is presented.

The *state* of the k-th droplet processed by the algorithm at frame N is noted D_N^k. The *state* gathers all the data relative to the position and the image of the drop at a given frame. Thus the set of droplets of frame N, D_N, is defined as $D_N = \left\{D_N^k, k \in \mathbf{N}\right\}$. And the k-th drop processed by the algorithm, D^k, is defined by $D^k = \left\{D_N^k, N \in \mathbf{N}\right\}$.

The first step of the algorithm consists in searching for the droplets D_N on the frame N+1. The droplets found are called *followed* because they are searched from their image on frame N. The detail of the *follow-up* is presented later.

In the presented example, the droplets D^k and D^{k+1} are found in the frame N+1. The droplets found give the *state* D_{N+1}^k and D_{N+1}^{k+1}. However the droplet D^{k+2} is not found by the tracking algorithm at frame N+1, this droplet is no longer searched by the algorithm.

The second step consists in *detecting* the droplets of the frame N+1. The set of droplets found by the *detection* are noted F_{N+1} and F_{N+1}^j is the j-th drop found in the frame N+1. The way droplets are *detected* is detailed below. It happens that droplets are tracked but not detected.

In the figure 1, the droplets *detected* are marked with dotted circles. All three droplets have been detected.

The third and last step consists in finding the new droplets among all the detected droplets. These new droplets form the set P_{N+1}. The *state* of these droplets is specified in order to add them to the set D_{N+1}.

In the example of the schema in figure 1, a new droplet is found. The position, the size and the image of this drop are finely determined in order to create the D_{N+1}^{k+3} element. This is the k+3th droplet processed by the algorithm.

Once this step is finished, the cycle continues with the set D_{N+1} to search in frame N+2.

The initialization of this algorithm at frame 1 is simply done by skipping the *follow-up* step because all the droplets present on the image are new.

The *follow-up* phase from one frame to another is not parallelizable. However, this step can be parallelized over all the droplets within a frame. Besides, the *detection* phase can be parallelized on all frames in order to accelerate the data processing before *follow-up*. The *follow-up* phase is the one that will limit the computation time.

2.3 Droplet *detection* method

The *detection* algorithm is detailed before the *follow-up* part because all the *followed up* droplets are previously *detected*.

In order to find the droplets on the image, a simplified image of them is used as a reference (see T_N^k figure 2). The radius and thickness of the simplified image can be changed to take into account potential variations of the image of the droplets on the camera.

A cross-correlation algorithm is then applied to find this simplified image on the whole image acquired by the camera. Only the local maxima of this correlation are retained.

To maximize the number of droplets detected and to minimize the false positives, a calibration phase of these parameters is necessary. The calibration is done on random images from the image bank to be processed to limit the selection bias.

The set of *detected* droplet positions at frame N will form the set P_N.

2.4 Method of *follow-up* droplets frame by frame

When a new droplet is *detected*, its *status* is specified as follows:

1. A set of simplified image is compared to the droplet to determine the best patch (T_N^k in Figure 2) and a 3-point quadratic interpolation is used to determine the apparent radius to sub-pixel accuracy. The best simplified image of a drop is denoted T_N^k

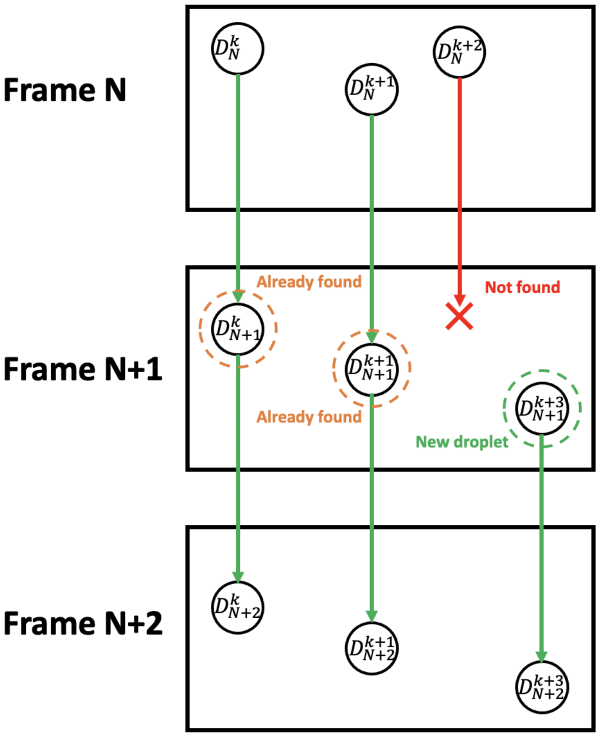

Fig. 1: Diagram illustrating the PTV algorithm from frame N to frame N+1.

2. This simplified image is centered with respect to the droplet at a sub-pixel precision thanks to a cross-phase correlation in order to precisely measure its position
3. The effective image of the drop is obtained by keeping only the signal inside the simplified image ($\tilde{I}^k_N$ on figure 2)

Thus, its position, the best simplified image, its image and its effective image are determined. These elements are included in the *state* of the drop and thus D^k_N. The I^k_N image and the $\tilde{I}^k_N$ effective image of the drop are samples of the slightly larger N frame of the image of the drop, as illustrated in figure 2.

The *follow-up* of the droplet D_k on frame N+1 from D^k_N is done as follows:

1. A sample S^k_{N+1} of the image size of I^k_N and at the same position as D^k_N is taken from frame N+1
2. A phase cross-correlation [6] is performed between S^k_{N+1} and $\tilde{I}^k_N$ to determine the droplet offset between frame N and frame N+1
3. Once the position of the drop is well determined, its *state* is specified to give D^k_{N+1}, as described above

The droplets only need to be *detected* once to start the *follow-up*. Thus, the *detection* algorithm does not need to find all the droplets on each image, this allows to relax the detection criteria and thus to limit the false positives.

2.5 Measurement of the number and position of interference fringes

Once the PTV algorithm is completed, the number and position of the interference fringes is measured. This work is done from the effective images $tildeI^k_N$:

1. $\tilde{I}^k_N$ is vertically averaged to obtain the interference signal
2. A 5th order Butterworth low pass filter is applied to smooth the signal. The filter is applied back and forth so that the initial phase is not modified
3. The signal undergoes a Fourier transform with a zero padding method to improve the accuracy (the signal length is increased 100 times)

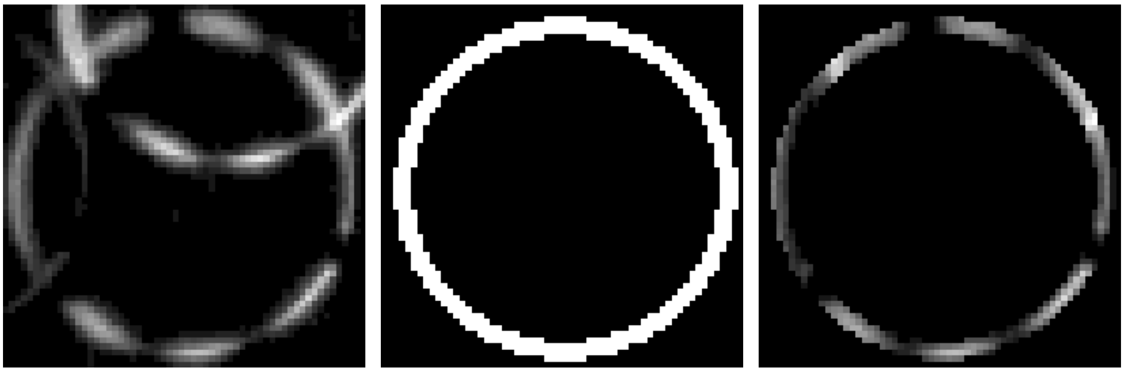

(a) I_N^k (b) T_N^k (c) $\tilde{I}_N^k$

Fig. 2: Example of a fuel drop image.

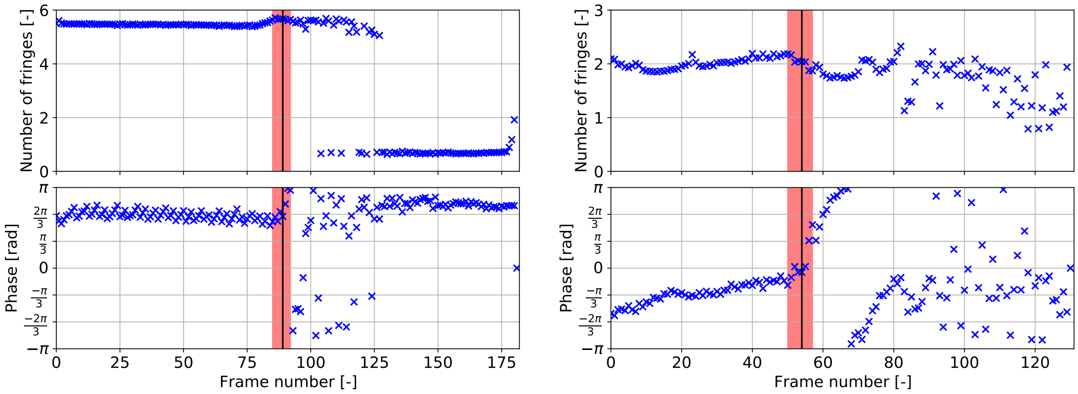

(a) Example with many fringe. (b) Example with few fringe.

Fig. 3: Example of the evolution of the number of fringes and the phase of the maximum FFT.

The number of fringes is then determined by the spatial mode given by the maximum of the Fourier transform. In addition, the phase associated with this peak is also measured to determine the position of the interference fringes. Thus, the position and the number of fringes are fully determined with precision.

These items can be added to the drop *status* and done during PTV tracking so that the actual $\tilde{I}_N^k$ images do not have to be saved. However, this may slow down the tracking. If all the effective images have been saved, this treatment can be done at the end since it is easily parallelizable.

2.6 Link between fringe position and evaporation

When the droplet evaporates its diameter decreases and therefore the positions of the intensity maxima and minima change. From the position of the fringes the instant when the droplet starts to evaporate is estimated as Wu did [23]. It is much simpler to estimate the beginning of evaporation from the position of the fringes than from the variation of the number of fringes as illustrated on the figure 3.

The positioning of the beginning of the evaporation is done manually. This manual action ensures that the evaporation is well positioned and that the droplet is not a false positive and is followed up until the evaporation process is over. The positioning of the beginning of evaporation is done so that the red band, of a width of 6 frames on the figure 3, contains the break of slope, the beginning of evaporation is given by the center of this band.

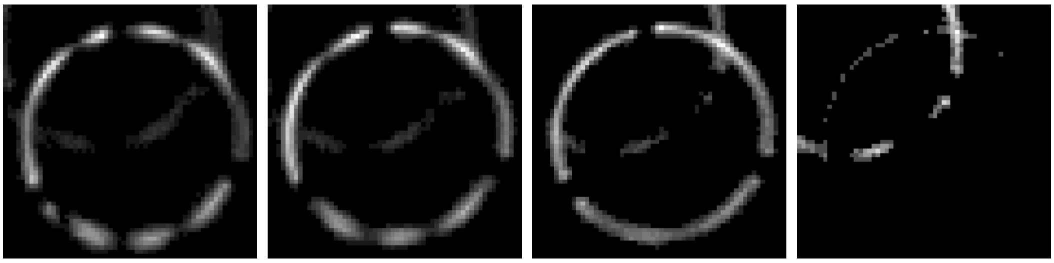

(a) $t = 0\,\mathrm{ms}$ (b) $t = 1.35\,\mathrm{ms}$ (c) $t = 2.7\,\mathrm{ms}$ (d) $t = 4\,\mathrm{ms}$

Fig. 4: Image of an evaporating droplet

2.7 Fast evaporation

In some case, the evaporation rate is so fast that it is no longer possible to measure the number of fringes. According to Wu [23] it is possible to measure a nanoscale change in diameter from the displacement of the interference fringes. He proposes the following formula:

$$\Delta D = \Delta\theta \frac{\lambda}{2\pi}\left(\sin\left(\frac{\phi}{2}\right) + \sqrt{n^2 + 1 - 2n\cos\left(\frac{\phi}{2}\right)}\right)^{-1} \tag{2}$$

with θ the phase associated with the spatial frequency of the fringes.

If the evaporation process is to fast, the image of the droplet is blurred and so the physical size of the droplet cannot be track during evaporation. The end of this section estimates in case of burnt gas the speed evaporation process and links it to the fringes position.

We can assume that a shift of the order of π of the fringes, i.e. when the maxima shift to the minima, during the exposure of the camera, makes it impossible to distinguish the interference fringes.

Let's anticipate the orders of magnitude of the experiment presented below to evaluate what is a fast evaporation. For a shift of π we have in the experiment $\Delta D = 0.22\,\mu\mathrm{m}$. The evaporation rate of dodecane at 1730 K was measured by Muelas [13] at $0.5348\,\mathrm{mm^2\,s^{-1}}$. Then for a 21.0 µm droplet, when half the mass is evaporated, the speed of regression of its surface is $16\,\mu\mathrm{m\,ms^{-1}}$, assuming that the surface of the droplet decrease linearly with time.

This means that if the exposure of the camera exceeds 14 µs, the fringes will be blurred.

To illustrate the result of the above calculations, the image of a droplet during its evaporation phase is presented in figure 4. This 20 µm droplet evaporates over 4 ms.

First, we can see that the fringes are clearly visible on both the *a* and *b* images, although it seems that on the *b* image the fringes are less clear because they move during the camera exposure.

However, on the image *c*, it is no longer possible to distinguish the fringes and thus to hope counting them. this image illustrates the blurred droplet's image in case of *fast* evaporation.

And finally, the image *d* shows a typical image of a droplet at the end of its life. The droplet is barely visible.

3 Experimental setup

3.1 Burner and optical diagnostics

The experimental setup chosen to apply the PTV diagnostic is the counterflow configuration (figure 5). A mixture of air and methane is injected from the bottom at an equivalence ratio of 0.9 with a Reynolds number of 1430 through an hole of 20 mm diameter. The top burner, similar to the bottom burner, injects air at Re = 950 containing a small amount of dodecane droplet ($6\,\mathrm{mg\,s^{-1}}$) so that the droplets evaporate on the hot front generated by the flame without disturbing the flow. The dodecane is injected by an ultrasonic injector fed by air and a syringe. The distance between the two burners is 52 mm. This configuration is protected by nitrogen co-flow.

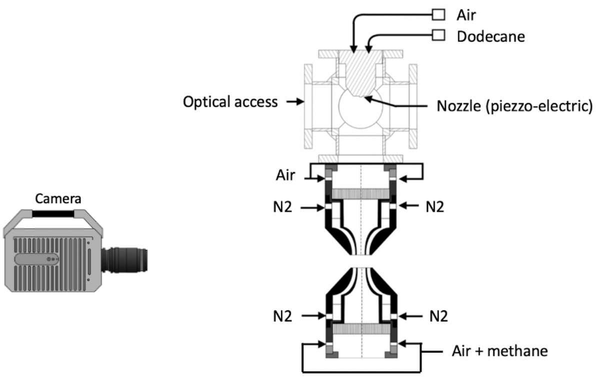

Fig. 5: Schematic representation of the experimental setup.

In order to carry out the diagnosis, a laser sheet of 1 mm is installed from a Verdi G continuous laser at 532 nm and a cylindrical lens. A camera, placed at 120°, acquires the images of the droplets at 20 kHz with a resolution of 720x504 pixels and an exposure time of 1/20 000 s. The camera is equipped by a Nikkon zoom f/2D 105 millim allowing to obtain a defocused image of the droplets. Moreover, between the zoom and the camera, an extension ring was installed with a special mask, presented above, to modify the droplets' image. In this experimental setup, 1 interference fringe stands for 4.9 µm, according to the formula proposed by Damaschke [4].

3.2 Characterization of the velocity and temperature field

In order to fully characterize the experimental setup, the 2D velocity and the temperature field in the laser sheet is measured.

3.2.1 Velocity field measurement

The velocity field shown in figure 6 was obtained by PIV measurement. Oil droplets of a few microns are injected in the top burner. These droplets are small enough to assume that their speed is identical to the flow. A laser with a 532 nm generates a laser sheet similar to the one used for the PTV to illuminate the droplets. These droplets evaporate at a temperature of 500 K, the end of the velocity field measurable by this technique shows this isotherm.

This isotherm was followed to determine the stability of the hot front and oscillates over a range of 0.5 millimeter around a stable position. This oscillation is slightly asymmetric with a slightly larger fluctuation for positive horizontal positions.

3.2.2 Temperature field measurement

The temperature field is measured by Rayleigh method [12]. A laser with 532 nm excites the gas in the burner and an intensified camera, placed perpendicularly to the laser sheet, acquires this signal. The signal intensity depends on the number and composition of gas within the laser sheet.

When the temperature increases, the density decreases and therefore the Rayleigh intensity decreases. From the diminution of the Rayleigh signal the temperature of the burnt gas can be measured. But the composition is slightly different and taking into account the presence of CO2, CO and H2O in the burnt gas, one can estimate that the signal ratio at the same temperature between the cold and burnt gas is 1.09.

In order to estimate the temperature in the burnt gas region and in the cold gas region, the laser beam have been focused toward these regions and the temperature were estimated from the signal intensity.

In the fresh gas the temperature is of 317 K and 1935 K in the burnt gas region with an uncertainty of the order of 50 K.

Then, from the local measurement, a 2D field of the temperature is measured in 3 steps :

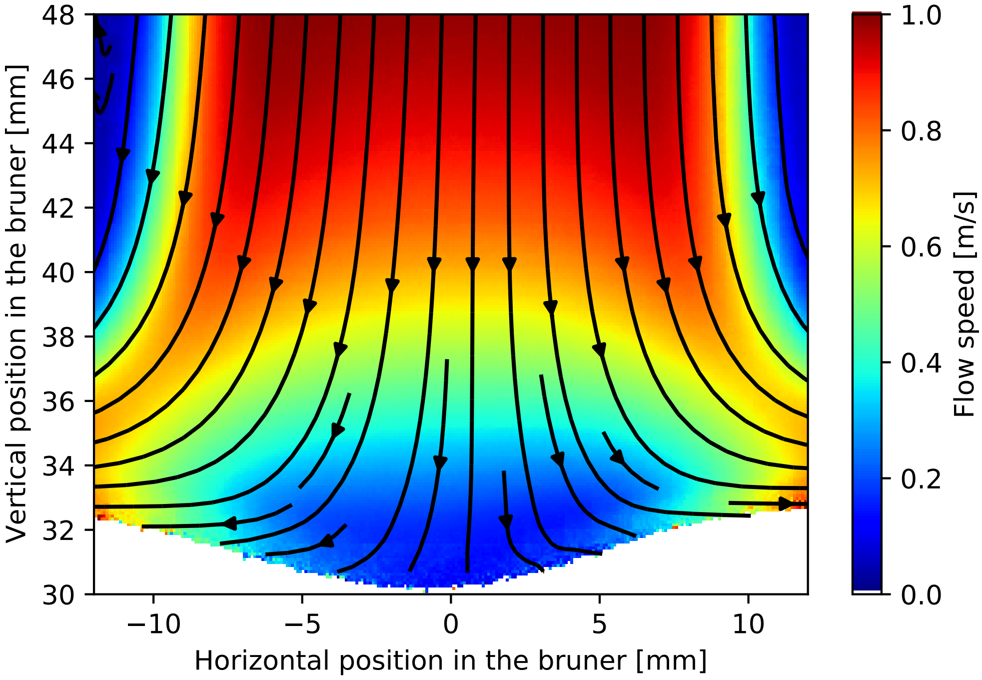

Fig. 6: 2D velocity map

1. A temperature field is determined by assuming that all gas has the same composition as fresh gas
2. From this field and assuming a unitary Lewis number, the 2D mixing field between fresh and burnt gases is determined
3. Thanks to this field of composition, a local temperature correction coefficient is evaluated

The correction being small, and the uncertainty high, it is not necessary to make several loops to obtain the result. Especially since this correction only affects the temperature gradient zone.

The resulting temperature field is shown in figure 7. The signal being very noisy, a low pass median filter was applied to reconstruct the temperature field with a spatial cutoff frequency of 0.6 mm.

We can see the shape of the warm front is similar to the shape of the isotherm obtained by measuring the velocity field in figure 7. However, the position of this front is different. The stable position of the flame depends on many parameters. Each time the flame is extinguished and then relit, it stabilizes on a new position. Thus, to ensure that the measurements are comparable, we waited for the flame to stabilize before making any measurements.

Finally, the temperature and velocity profile along the axis of symmetry have been drawn on the same graph from the velocity field isotherm (figure 8). The 2D environment in which the droplets evolves is reconstituted.

4 Experimental results

4.1 Droplet selection process

Following the 20,000 processed images of evaporating droplets, 105 droplets are retained among all. More droplets were found but a part of them were rejected for the following reasons:

- Not visible on more than 100 consecutive images
- Impossible to clearly identify the evaporation phase
- Clear break in the intensity of the droplets

The purpose of these criteria is to select the droplets that evaporate into the laser sheet.

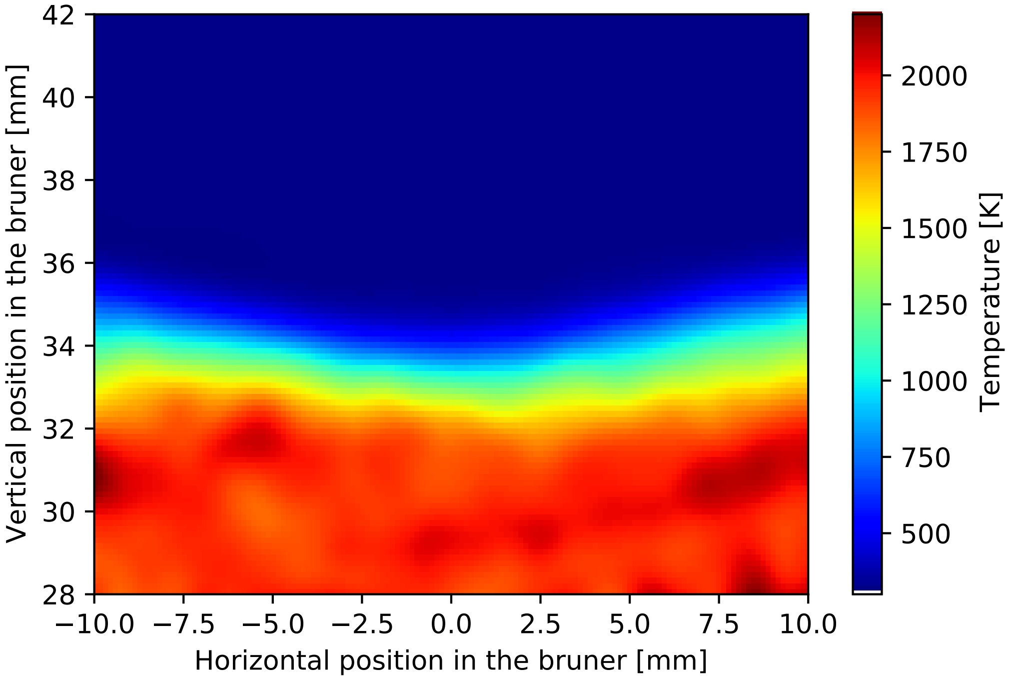

Fig. 7: 2D temperature map

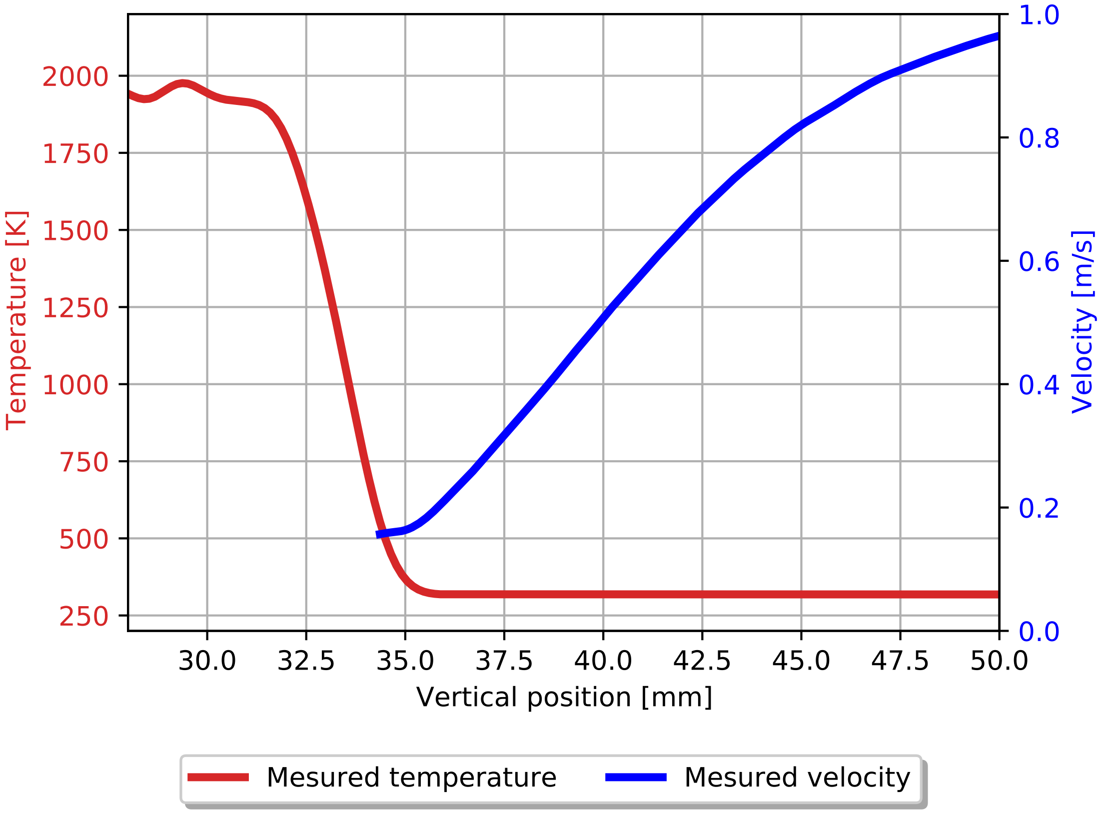

Fig. 8: Velocity and temperature along the burner axis.

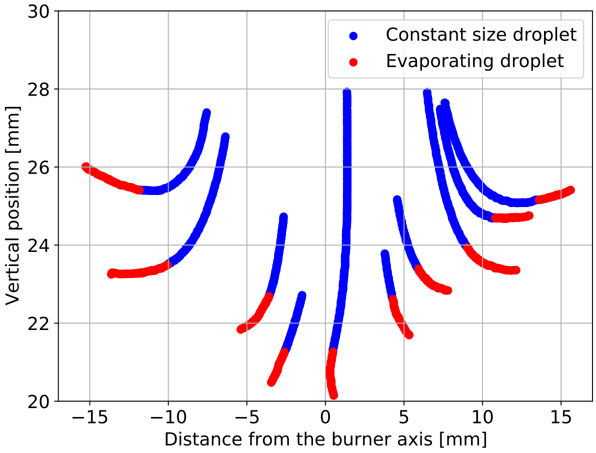

Fig. 9: 10 droplets' trajectory

The majority of the measured droplets are tracked over approximately 300 images. In addition, each selected droplet is manually checked to ensure that the tracking is correct.

The clear break in the intensity criteria stands for droplets leaving the laser sheet. Most of the droplets rejected for this criteria have, in the worst case, barely started their evaporation before disappearing.

4.2 Sizes and trajectories obtained by the presented PTV algorithm

Figure 9 shows the trajectory of 10 droplets selected among the 105 droplets to illustrate the typical trajectories obtained by PTV.

The measured trajectories match the expected ones in this configuration [9], as well as for the evaporation location.

The uncertainty on the initial time of evaporation is 0.15 ms as shown in figure 3 since this time is position with 3 frames uncertainties and the sampling rate is 20 kHz.

Regarding the final time of evaporation, its estimation is be based on the d2 law[1] and the mean fringes intensity over the last millisecond. Droplets with a Mie parameter greater than 10 emit a signal proportional to the diameter squared [22] (droplets bigger than 1.7 microm in the present work). Assuming that during the last millisecond, the signal remains proportional to the diameter squared and that the evaporation follows the d2 law, we can estimate the end of life of the droplet. The end of evaporation with this method is almost the same as the vanishing of the droplets from the frames with an average discrepancy of 0.15 ms.

On the overall, the total evaporation delay uncertainty is estimated at 0.3 ms.

Figure 10 shows the distribution of initial droplet diameter and suggests that the method does not favor any droplet size. The Sauter mean diameter is 21.0 µm and the diameter uncertainty is 2 µm from the work done on the effect of burnt gases.

4.3 Relevance of the algorithm compared to a classical PTV algorithm

A classical PTV algorithm is done in two steps: First, it *detects* the droplets on the set of images, then from the *detected* droplets it recreates trajectories. In the case of the present work, it means that the trajectories would be based only on the set of F_N.

Let's show that the set of droplets *detected* in F_N decreases greatly during the evaporation process. For this purpose let's define the error rate Er which is the number of *tracked* droplets that are not detected:

$$Er = 1 - \frac{|\bigcup_{N \in \mathbf{N}} F_N \cap D_N|}{|\bigcup_{N \in \mathbf{N}} D_N|} \tag{3}$$

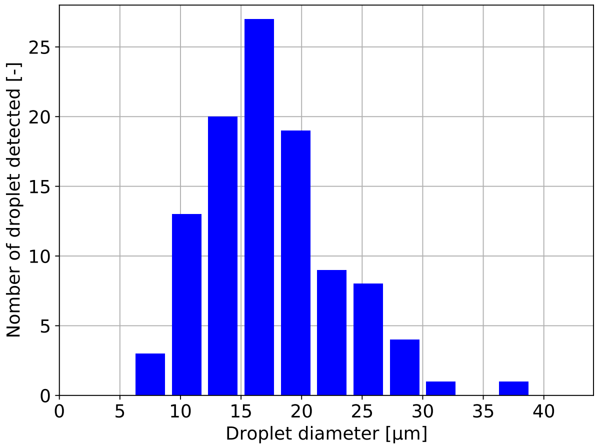

Fig. 10: Distribution of measured drop diameters

This error rate is evaluated on the 105 droplets obtained by our PTV algorithm. First, if only the states where the droplets do not evaporate is considered for the error calculation (blue part of the trajectories in the figure 9), the error rate is 25 %. This shows that the vast majority of non evaporating droplets *followed-up* are also *detected*. And so, a classical PTV algorithm is perfectly fine for non evaporating droplets.

However, when the droplets evaporate (red part of the trajectories in the figure 9) this error rate increases up to 65%. This shows that without the *follow-up* phase, there is a risk of missing the evaporation phase. Especially since the error rate rises to 91% during the last millisecond (20 lasts points of the red part of the trajectories in the figure 9). Thus, relying only on the detected droplets it is not possible to correctly follow the evaporating droplets.

This shows the interest of the *followed-up* phase and what this phase brings in the case of droplets with a great variety of intensity and some of which are in full evaporation.

4.4 Characteristic evaporation time

The evaporation is measured the time spent between the beginning of evaporation and the vanishing of the droplets. The figure 11 shows the evaporation time of the droplets as a function of their initial diameter.

The order of magnitude related to the evaporation delay is consistent with the estimation in part 3. The delay is slightly larger because the droplets start to evaporate before entering in the burnt gas and therefore evaporate at a lower average temperature. The larger droplets evaporate more slowly because they are heavier, which explains the increase of the overall evaporation delay with the droplets diameter.

A dispersion in evaporation delay is observed. This dispersion is larger than the uncertainty on the evaporation time of the droplets. The dispersion may be due to the slight instability of the heat front.

4.5 Evaporation characteristic distance

As the droplets are followed during their evaporation phase, the distance over which they evaporate is also measured. The evaporation distance as a function of the initial diameter of the droplets is plotted in figure 11.

As for the evaporation time, a dispersion on the evaporation distance can be observed. The dispersion is related with the distance from the burner axis during the evaporation process. When the size of the droplets is fixed, a greater distance to the burner axis leads to a greater evaporation distance. Indeed, the more the droplet is far from the axis the more the horizontal flow is important and so the drag force. Thus, this leads to an increase in the evaporation distance, since the droplets are carry by the horizontal flow over a larger distance.

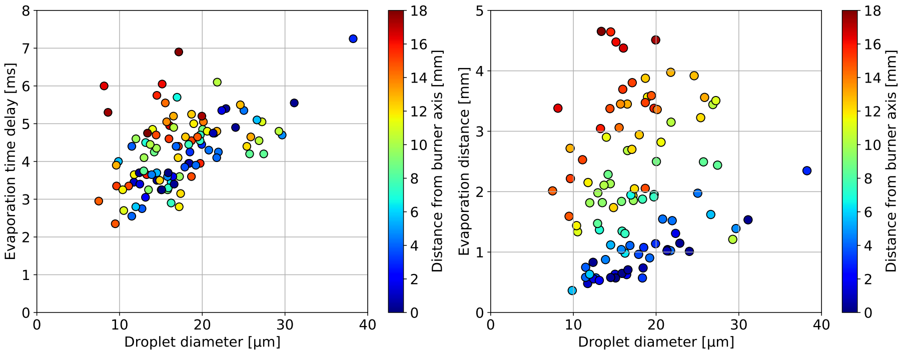

(a) Characteristic evaporation time delay (b) Evaporation characteristic distance

Fig. 11: Data collected during the measurement campaign. Each point represents a drop and these are related by their eccentricity during their evaporation phase.

At a given a distance from the burner axis, the evaporation distance increases with the droplets' size. Indeed, bigger droplets takes more time to evaporate and therefore travels a greater distance. Moreover, these drops being initially larger, they have a greater inertia and thus have a greater speed during the evaporation phase.

5 Measurements with the bottom burner offset from the top burner to evaluate the effect of the burnt gases

5.1 Measurement setup and methodology

Burnt gas are present on the optical path between the droplets and the camera. This part assesses the effect of the burnt gas on the image of the droplets.

The setup selected for this purpose is the same as above but with the bottom burner at mid-distance between the top burner and the camera. This configuration is presented in figure 13, with a distance between the camera and the top burner of about 30 cm and of 15 cm for the bottom burner. In this setup there is burnt gas on the optical path between the droplets and the camera without affecting the droplets.

The velocity field of this configuration is measured by PIV and is presented in figure 12. Let's estimate the accuracy of the PTV measurement by assuming that the droplets have a constant velocity and diameter because they are only carried in a vertical flow at room temperature.

In this configuration, 3000 images were acquired with the bottom burner turned off and 3000 images with burner turned on.

The objective is to determine the deviation of the horizontal and vertical position as well as the position and number of fringes with respect to the assumptions made above. The parameters of the PTV algorithm are identical as for the case of evaporating droplets with the burners facing each other.

5.2 Data collected during the measurement

When the bottom burner is turned off, the algorithm found 85 droplets, 68 were real droplets. In contrast to the measure where the droplets evaporate, there is a large number of false positives, here 20%. In this setup, the top burner is not heated by the flame, so it is colder. This low temperature increases the number of droplets that reaches the measurement area, because they do not evaporate on the way. And so, this high density of droplets generates a greater quantity of false positives. These 68 droplets are used to determine the uncertainty of measurement on the position of the droplets.

Among these 68 droplets, there are 58 for which it is possible to correctly measure the diameter during at least 50 consecutive images. We use the images where it is clearly possible to measure

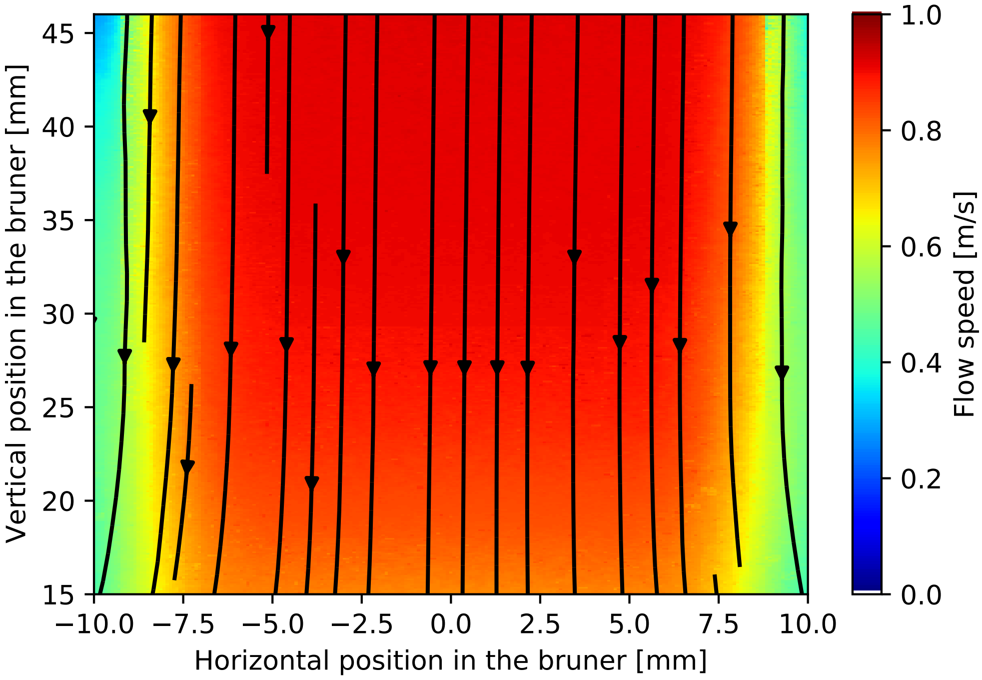

Fig. 12: Veocity map for the offset burner configuration.

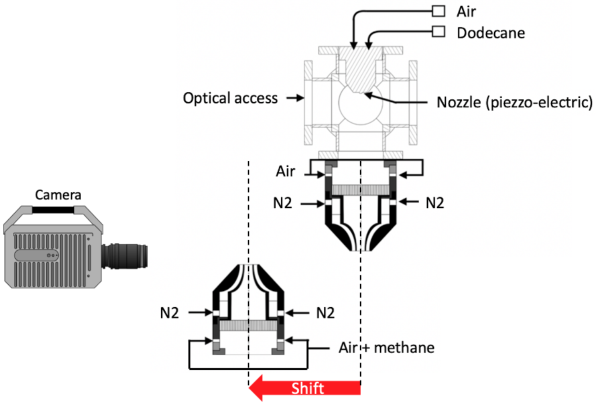

Fig. 13: Scheme of the offset burner configuration.

the number of fringes to estimate the accuracy on the position and the number of fringes. The SMD of these droplets is 17.1 microm.

When the bottom burner is lit, 88 droplets are found with 65 exploitable trajectories. And among these exploitable trajectories, it is possible to measure the number and the position of fringes on 44 of these droplets. The smd of the droplets thus obtained is 16.6 microm.

This allows us to see that the data obtained is comparable and that the same thing is measured in both cases. The burnt gases do not seem to significantly affect the amount of data acquired.

5.3 Limit of the measurement

The dispersion of the measurements with respect to the previously stated hypotheses is presented in the table 1. In this table, the number of points which allowed to determine this standard deviation is specified between brackets:

We can see that the accuracy of the trajectory is not affected by the burnt gases. The uncertainty remains around 0.1 pixels. Indeed, the effect of the burnt gases generates fluctuations with

	Sans flamme	Avec flamme
Position horizontale [pixel]	0.119 (20193)	0.0922 (17537)
Position verticale [pixel]	0.116 (20193)	0.105 (17537)
Nombre de franges [-]	0.135 (9374)	0.227 (9413)
Phase [rad]	0.312 (9374)	0.375 (9413)

Table 1: Dispersion of the measured values in the offset burner configuration.

characteristic times greater than the sampling time and therefore the trajectory manages to remain globally stable.

On the other hand, the burnt gases affects the interference signal and therefore the precision on the number of fringes decreases, as well as on the position of the fringes. When the burnt gases disturb the droplet's signal, its image is distorted and therefore it is more difficult to measure its size and to extract the signal from the fringes. Nevertheless, the extrema remain correctly positionable, which explains why the effect on the phase is less important than on the fringes.

6 Conclusion

The present work managed to introduce a new PTV algorithm to measure evaporation time delay and length near a flame of fast evaporating droplets. It adapted ILIDS measurement with a high frequency PTV tracking to follow the evaporation of droplets.

The start of the evaporation process was determined from nanoscale change in diameter of the droplets obtained from the position of the fringes. Then during the evaporation, ILIDS was no longer possible since fringes are not stable enough and so it was not possible to estimate the evaporation delay from the droplets' diameter decrease. However, thanks to the new PTV algorithm, this delay were measured since the droplets were followed during their whole evaporation process.

Thus, in addition to the information on the number of fringes, their position has been exploited to determine the beginning of the evaporation process. Measuring the evaporation from allows to estimate the beginning of the evaporation more simply than by looking at the decrease of the number of fringes. Moreover, it is very difficult to follow the evolution of the number of fringes during the evaporation process, because they are not fixed during the exposure of the camera. Nevertheless, the effect of the environment could be evaluated, in particular the effect of the burnt gases and it could be shown that the dispersion of the measured quantities remains very reasonable.

Finally, the length and the characteristic time of evaporation could be measured. A very strong dispersion of the evaporation lengths could be observed, but it seems that this can be explained in large part by the eccentricity of the drops.

Thanks to this new technique, we hope that it will be possible to measure and observe new phenomena thanks to this Lagrangian tracking of fuel droplets.

References

1. By D B Spalding. COMBUSTION OF LIQUID FUELS 847 Symbol a B b THE COMBUSTION OF LIQUID FUELS. *Symposium (international) on combustion*, 4:847–864, 1953.
2. R. Baudoin and L. Zimmer. Procédé et système optique de détection de particules dans un écoulement, 12 2015.
3. Christian Chauveau, Fabien Halter, A Lalonde, and Iskender Gökalp. An experimental study on the droplet vaporization: effects of heat conduction through the support fiber. IT 2008. (May 2015):8–10, 2008.
4. Nils Damaschke, Holger Nobach, Thomas I. Nonn, Nikolay Semidetnov, and Cameron Tropea. Multi-dimensional particle sizing techniques. *Experiments in Fluids*, 39(2):336–350, 2005.
5. Hojat Ghassemi, Seung Wook Baek, and Qasim Sarwar Khan. Experimental study on evaporation of kerosene droplets at elevated pressures and temperatures. *Combustion Science and Technology*, 178(9):1669–1684, 2006.
6. Manuel Guizar-Sicairos, Samuel T. Thurman, and James R. Fienup. Efficient subpixel image registration algorithms. *Optics Letters*, 33(2):156, 2008.
7. Yannis Hardalupas, Srikrishna Sahu, Alex M.K.P. Taylor, and Konstantinos Zarogoulidis. Simultaneous planar measurement of droplet velocity and size with gas phase velocities in a spray by combined ILIDS and PIV techniques. *Experiments in Fluids*, 49(2):417–434, 2010.
8. G. König, K. Anders, and A. Frohn. A new light-scattering technique to measure the diameter of periodically generated moving droplets. *Journal of Aerosol Science*, 17(2):157–167, 1986.
9. Amable Liñán, Daniel Martínez-Ruiz, Antonio L. Sánchez, and Javier Urzay. Regimes of spray vaporization and combustion in counterflow configurations. *Combustion Science and Technology*, 187(1-2):103–131, 2015.

10. M. Maeda, Y. Akasaka, and T. Kawaguchi. Improvements of the interferometric technique for simultaneous measurement of droplet size and velocity vector field and its application to a transient spray. *Experiments in Fluids*, 33(1):125–134, 2002.
11. Masanobu Maeda, Tatsuya Kawaguchi, and Koichi Hishida. Novel interferometric measurement of size and velocity distributions of spherical particles in fluid flows. *Measurement Science and Technology*, 11(12), 2000.
12. A. R. Masri, R. W. Dibble, and R. S. Barlow. The structure of turbulent nonpremixed flames revealed by Raman-Rayleigh-Lif measurements. *Progress in Energy and Combustion Science*, 22(4):307–362, 1996.
13. Álvaro Muelas, Jaime Carpio, Javier Ballester, Antonio L. Sánchez, and Forman A. Williams. Pyrolysis effects during high-temperature vaporization of alkane droplets. *Combustion and Flame*, 217:38–47, 2020.
14. Hiroshi Nomura, Yasushige Ujiie, Hans J. Rath, Jun'ich Sato, and Michikata Kono. Experimental study on high-pressure droplet evaporation using microgravity conditions. *Symposium (International) on Combustion*, 26(1):1267–1273, 1996.
15. Y. Park, G. Choi, and L. Zimmer. Experimental study of the dynamics of pulsated laminar counter-flow spray flames using optical flow and proper orthogonal decomposition. *COMODIA 2017 - 9th International Conference on Modeling and Diagnostics for Advanved Engine Systems*, (Comodia), 2017.
16. Lu Qieni, Han Kan, Ge Baozhen, and Wang Xiang. High-accuracy simultaneous measurement of particle size and location using interferometric out-of-focus imaging. *Optics Express*, 24(15):16530, 2016.
17. A. Querel, P. Lemaitre, M. Brunel, E. Porcheron, and G. Gréhan. Real-time global interferometric laser imaging for the droplet sizing (ILIDS) algorithm for airborne research. *Measurement Science and Technology*, 21(1), 2010.
18. Raffaele Ragucci, Antonio Cavaliere, and Patrizio Massoli. Drop Sizing by Laser Light Scattring Exploiting Intensity Angular Oscillation in the mie regime. *Particle Particle Systems Characterization*, 7(1-4):221–225, 1990.
19. Weiwei Shang, Shouyin Yang, Tiemin Xuan, Zhixia He, and Jiawei Cao. Experimental Studies on Combustion and Microexplosion Characteristics of N-Alkane Droplets. *Energy and Fuels*, 2020.
20. Michael Stöhr, Stephan Ruoff, Bastian Rauch, Wolfgang Meier, and Patrick Le Clercq. Droplet vaporization for conventional and alternative jet fuels at realistic temperature conditions: Systematic measurements and numerical modeling. *Proceedings of the Combustion Institute*, 000:1–8, 2020.
21. R. Thimothée, C. Chauveau, F. Halter, and I. Gökalp. Experimental investigation of the passage of fuel droplets through a spherical two-phase flame. *Proceedings of the Combustion Institute*, 36(2):2549–2557, 2017.
22. Cameron Tropea. Optical particle characterization in flows. *Annual Review of Fluid Mechanics*, 43:399–426, 2011.
23. Yingchun Wu, Haipeng Li, Marc Brunel, Jia Chen, Gérard Gréhan, and Lutz Mädler. Phase interferometric particle imaging for simultaneous measurements of evaporating micron-sized droplet and nanoscale size changes. *Applied Physics Letters*, 111(4), 2017.